CSIRO PUBLISHING
www.publish.csiro.au/journals/eg
Exploration Geophysics, 2007, **38**, 1–18

Numerical studies of information about elastic parameter sets in non-linear elastic wavefield inversion schemes

Akio Sakai

Japan Petroleum Exploration Co. (Japex), 2-2-20 Higashi-shinagawa, Shinagawa, Tokyo 140-0002, Japan.
E-mail: akios@japex.co.jp

Abstract. Non-linear elastic wavefield inversion is a powerful method for estimating elastic parameters for physical constraints that determine subsurface rock and properties. Here, I introduce six elastic-wave velocity models by reconstructing elastic-wave velocity variations from real data and a 2D elastic-wave velocity model. Reflection seismic data information is often decoupled into short and long wavelength components. The local search method has difficulty in estimating the longer wavelength velocity if the starting model is far from the true model, and source frequencies are then changed from lower to higher bands (as in the 'frequency-cascade scheme') to estimate model elastic parameters. Elastic parameters are inverted at each inversion step ('simultaneous mode') with a starting model of linear P- and S-wave velocity trends with depth. Elastic parameters are also derived by inversion in three other modes – using a P- and S-wave velocity basis ('V_P V_S mode'); P-impedance and Poisson's ratio basis ('I_P Poisson mode'); and P- and S-impedance ('I_P I_S mode'). Density values are updated at each elastic inversion step under three assumptions in each mode. By evaluating the accuracy of the inversion for each parameter set for elastic models, it can be concluded that there is no specific difference between the inversion results for the V_P V_S mode and the I_P Poisson mode. The same conclusion is expected for the I_P I_S mode, too. This gives us a sound basis for full wavelength elastic wavefield inversion.

Key words: non-linear elastic wavefield inversion, frequency-cascade scheme, simultaneous mode, gas hydrate.

Introduction

An elastic model is described by three independent parameters, such as the Lamé constants λ, μ and mass density ρ. There is a reliability gap in reflection seismology between P-wave velocity information, associated with traveltimes, providing the longer wavelength part of velocity structures, and reflectivity information estimated from P-impedances at shorter wavelength (Claerbout, 1985). Dębski and Tarantola (1995) discussed the information in possible elastic parameter sets for one-layer models derived from the amplitudes of reflected waves. They concluded that P-impedance, Poisson's ratio, and mass density constitutes the best resolved parameter set when inverting seismic amplitude variation with offset. They inverted a simple velocity model, and did not discuss the problem of retrieving a longer-wavelength velocity model, constrained by the arrival times of reflected waves. I now examine cases of complex velocity structures, to search for the best elastic parameter set in a full wavelength inversion approach. The term 'full wavelength elastic inversion' here means the attempt to retrieve the spatial distribution of elastic parameters at all wavenumbers. It has been a difficult task to estimate the longer wavelength distribution of elastic parameters, compared with the shorter wavelength distribution, using the elastic wavefield inversion approach (e.g. Mora, 1988).

The purpose of the current research is to focus on the problem to examine which set or combination of elastic parameters shows the maximum information in non-linear elastic wavefield inversion at all wavelengths. By maximum information, I mean the most accurate result among the combination of elastic parameters estimated by non-linear elastic wavefield inversion. Several elastic models are constructed from a model based on the gas hydrate and gas bearing logging data in the Nankai Trough (Sakai, 2000, 2003). The computation accuracy in inversion is evaluated for several 1D and 2D models for each set of elastic parameters under several density constraints and ambient noise conditions. From this examination, it is concluded that there is no advantage in selecting P-impedance, Poisson's ratio, and density over the P-wave velocity, S-wave velocity, and density set, in the present full-wavelength inversion scheme. The same conclusion is expected for the P-impedance, S-impedance, and density set, although the number of inversion trials is smaller than for the other modes in this study.

Elastic-wave velocity estimates for physical properties

Elastic-wave velocity is the basic physical quantity for solid and fluid identification in exploration for hydrocarbons and gas hydrates, and for monitoring of injected carbon dioxide in geologic sequestration. Non-linear elastic wavefield inversion is an iterative computational attempt to provide elastic-wave velocity estimates for which synthetic traces most closely resemble observed traces. Standard velocity analysis methods based on image enhancing principles, such as stacking velocity analysis and pre-stack migration, have limited resolution and accuracy, and are usually restricted to estimation of P-wave velocity. Amplitude variation with offset techniques assume overburden elastic-wave velocity structure and have difficulties with thin or curved layer estimates. The reliability of the analyses in such cases remains dubious.

There are many examples that show the benefit of the application of elastic-wave velocity to estimation of physical properties. A first example is the seismic monitoring of carbon dioxide injection. To mitigate the problem of global climate change, the geological sequestration of carbon dioxide is being tested by injecting carbon dioxide into saline aquifers and depleted oil and gas fields (e.g. Arts et al., 2002). To observe the extent and effect of the injected carbon dioxide, elastic-

10.1071/EG07011 0812-3985/07/010001

wave velocity can be utilised to estimate the saturation and pore pressure of the carbon dioxide. The influence of the effective pressure on the V_P versus V_P/V_S relation for water-saturated clean sand sediment can be obtained from a rock physics model (Dvorkin et al., 1999; Sakai, 1999), illustrated in Figure 1.

A second example is the estimation of saturation of natural gas hydrates. Gas hydrate is an ice-like clathrate compound, stable under low temperature and high pressure conditions. Naturally occurring gas hydrates in deep marine and permafrost sediments control the global near-surface carbon budget and are beginning to be explored as possible future fossil fuel resources. Two opposing gas hydrate reservoir models have been proposed from rock physics, tentatively called the compaction model and the cementation model (Dvorkin et al., 1999; Sakai, 1999). Research using reliable elastic-wave velocity data show that the compaction model proves to be a universal model in both permafrost and deep marine sediment (e.g. Sakai, 1999, 2000). For the compaction model, the V_P versus V_P/V_S relation in case of clean sand sediment is illustrated as a function of porosity (ϕ) and gas hydrate saturation (Sh) in Figure 2.

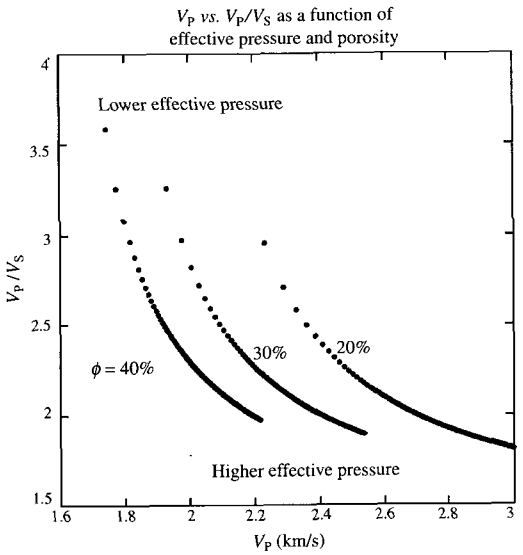

Fig. 1. V_P versus V_P/V_S relation for effective pressure estimate.

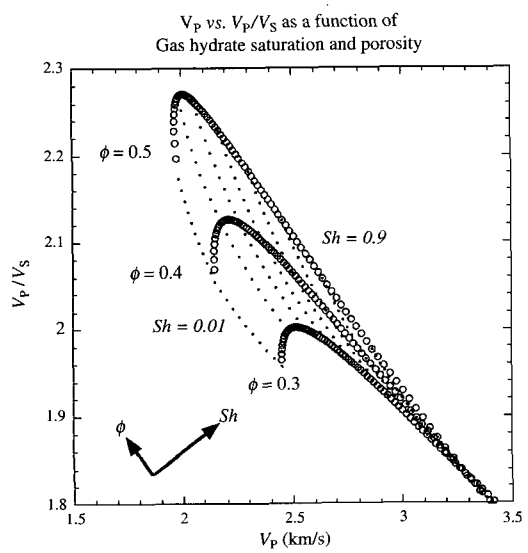

Fig. 2. V_P versus V_P/V_S relation for gas hydrate saturation estimate.

I have given two examples to show the importance of elastic-wave velocity estimates. There have been studies of acoustic or elastic wavefield inversion for estimation of fine P-wave velocity structures. In analysis of real rock physics data, several combinations of elastic parameters can be taken for interpretation, such as Lamé constants, impedances, Poisson's ratio, and others. Each elastic parameter set is invertible by mathematical operation and the sets are mathematically identical. If the accuracy of inversion results is independent of the choice of unknown elastic parameter sets, the elastic wavefield inversion method will provide a sound basis for subsequent interpretation of any parameter sets.

In the current research, the elastic-wave velocity model for inversion is constructed from logging data from a well in the Nankai Trough, offshore Japan, acquired in the 1999 MITI drilling campaign (See Figure 3a for well location). The P-wave

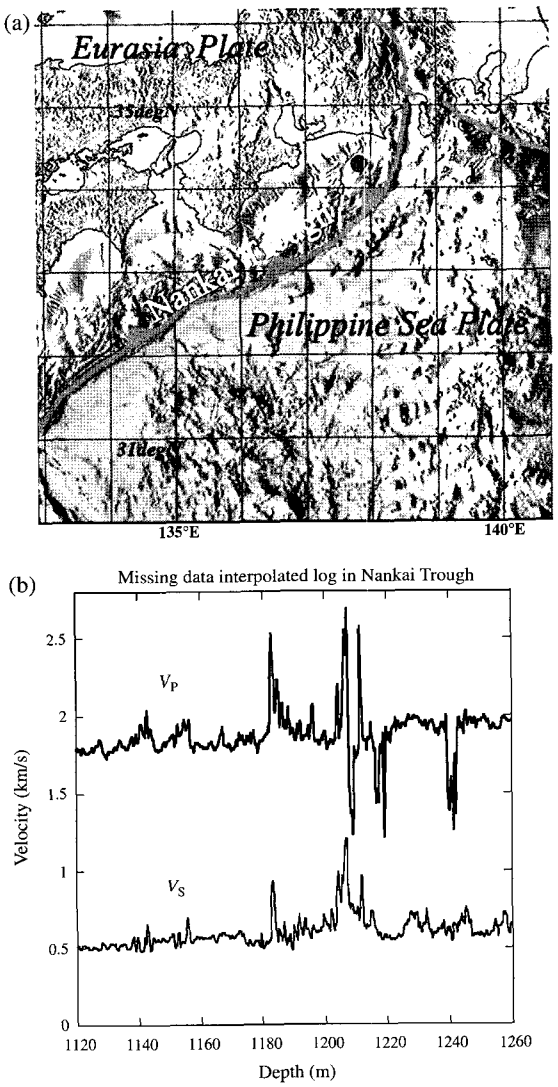

Fig. 3. (a) Location map of a MITI Nankai Trough well offshore Japan. Well location is shown as a dot on the map. (b) Logging data from a well in the Nankai Trough (Upper figure: P-wave velocity data, lower figure: S-wave velocity). In the depth intervals of 1208–1210 m, 1215–1217 m, 1219–1220 m, and 1239–1242 m, V_P data were not observed due to high attenuation of the first arrivals in Schlumberger's DSI tool. Higher V_P and V_S are interpreted as gas hydrate saturated zones such in the depth intervals of 1139–1145 m, 1150–1155 m, 1182–1190 m, and 1203–1212 m. Missing V_P data were interpolated after wavefield inversion of VSP with gas saturation estimates (after Sakai, 2000, 2003).

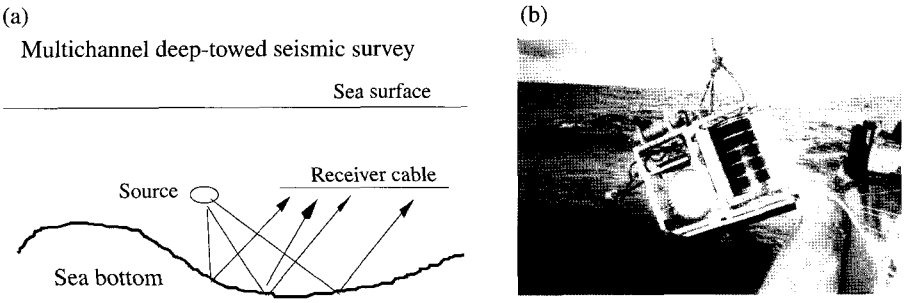

Fig. 4. (a) Schematic configurations of deep-towed seismic survey. (b) The Helmholtz transducer source about to submerge at the stern of MV Kaiko Maru 7 for the first shot at the DTAGS 1997 survey in the Nankai Trough.

velocity log data were missing over four depth intervals. Values in these intervals were interpolated by estimating P-wave velocity using elastic wavefield inversion of vertical seismic profile (VSP) data (Sakai, 2000, 2003). At the same time, the quantity of gas was also evaluated for log data estimates in the missing zones. The estimated P-wave velocity distribution is shown in Figure 3b. Elastic-wave velocity data, after filling missing zones in this well, were resampled at 1-m spacing, which is used as the key model in evaluating the inversion accuracy in several elastic parameter sets. Velocity fluctuations in the key model are used to construct five other models with different statistics, evaluating the inversion accuracy over a wide variety of elastic parameter fluctuations in depth.

Implementation

The non-dissipative elastic wavefield is governed by a linear first-order coupled equation for particle velocity and stress in Cartesian coordinates. Computed results are derived from a two-dimensional finite-difference method with a second-order accurate time and fourth-order accurate space formulation of the staggered-grid scheme (Levander, 1988). In this study, source and receivers are located in the water, and pressure is measured at the receivers. The present inversion method can be applied to any type of marine seismic survey such as ocean-bottom seismometer, ocean-bottom cable, VSP, and deep-towed seismic systems as well as conventional multi-channel seismic surveys. As an example of such a deep-towed system, the Deep Towed Acoustics/Geophysics System (DTAGS) of the USA's Naval Research Laboratory was used in a survey conducted offshore Japan in 1997 for gas hydrate research (see Figure 4; Sakai, 1998).

The non-linear elastic wavefield inversion scheme now in use is essentially based on the iterative search method of Tarantola (1986), utilising the local gradients of the misfit function. The misfit function is defined by the least-squared difference functional (L_2 norm) between the observed data and the synthetic data over receivers and shots at all time samples:

$$E = \sum_{shots} \int \mathrm{d}t C_d^{-1} \sum_{receivers} |S_{\mathrm{syn}} - S_{\mathrm{obs}}|^2 + \Delta m^{\mathrm{T}} C_m^{-1} \Delta m \qquad (1)$$

$$E = \sum_{shots} \int \mathrm{d}t \sum_{receivers} |S_{\mathrm{syn}} - S_{\mathrm{obs}}|^2 \qquad (2)$$

where S_{syn} is the current synthetic wavefield and S_{obs} is the observed seismic data, Δm is the residual of the current model and the superscript T indicates the transpose. The a priori data covariance matrix C_d is set to unity by normalising the data. The model covariance matrix C_m term is used to smooth out changes of the model parameters close to the minimum point. Assuming nominally an infinite a priori variance in the model space here, the C_m term is disregarded in the misfit function representation, as the inversion turns out to be stable without damping. The inversion is driven to minimise the misfit function in the model space. The gradient direction of the steepest descent g_n indicates the direction of the most rapid change of the misfit function in the neighbourhood of the starting model and is computed by back-propagating the data residuals and correlating the result with the forward-propagated wavefield (Lailly, 1983; Tarantola, 1984). Gradients with respect to the Lamé constant set and density are represented by velocity and stress tensors as follows. The forward wavefield is denoted by the forward vector arrow, and the backward wavefield is denoted by the backward vector arrow:

$$\begin{aligned}
\delta\hat{\lambda} &= -\frac{1}{4(\lambda+\mu)^2} \sum_{shots} \int \mathrm{d}t (\vec{\tau}_{xx} + \vec{\tau}_{zz})(\vec{\tau}_{xx} + \vec{\tau}_{zz}) \\
\delta\hat{\mu} &= \frac{\lambda(\lambda+2\mu)}{4\mu^2(\lambda+\mu)^2} \sum_{shots} \int \mathrm{d}t (\vec{\tau}_{xx}\vec{\tau}_{zz} + \vec{\tau}_{zz}\vec{\tau}_{xx}) \\
&\quad - \frac{\lambda^2 + (\lambda+2\mu)^2}{8\mu^2(\lambda+\mu)^2} \sum_{shots} \int \mathrm{d}t (\vec{\tau}_{xx}\vec{\tau}_{xx} + \vec{\tau}_{zz}\vec{\tau}_{zz}) \qquad (3) \\
&\quad - \frac{1}{\mu^2} \sum_{shots} \int \mathrm{d}t \vec{\tau}_{xz}\vec{\tau}_{xz} \\
\delta\hat{\rho} &= -\sum_{shots} \int \mathrm{d}t \left(\vec{u}_x \frac{\delta^2 \vec{u}_x}{\delta t^2} + \vec{u}_z \frac{\delta^2 \vec{u}_z}{\delta t^2} \right)
\end{aligned}$$

If the model vector m_n and step length α_n at the n-th inversion step is given, then the model vector is updated to reduce the misfit function in a step-by-step line-search mode. Preconditioning by a finite a priori model covariance matrix is combined with

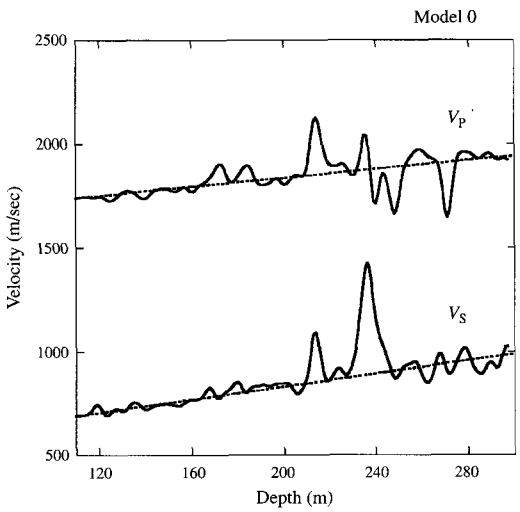

Fig. 5. Elastic-wave velocity model of Model 0 (thick curves) and the starting model for inversion (dashed curves).

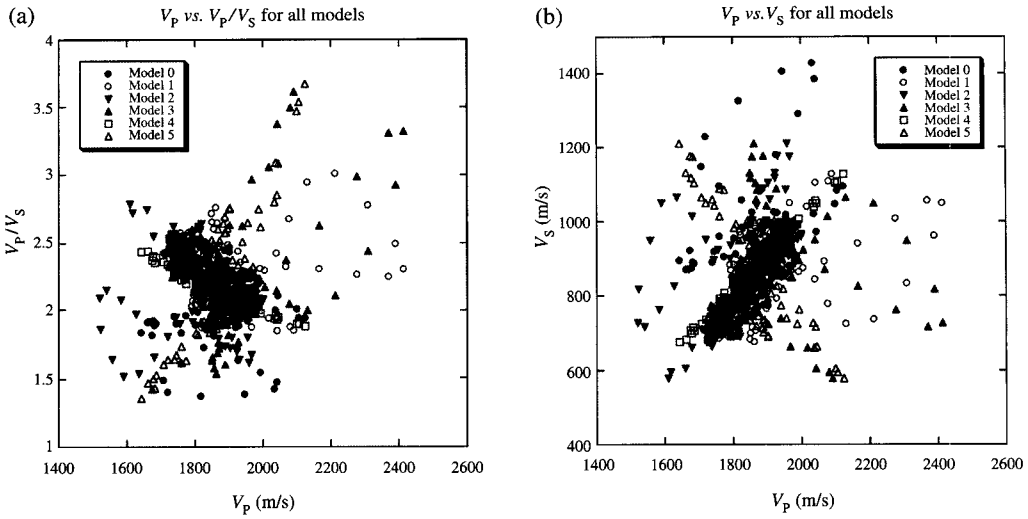

Fig. 6. (a) V_P versus V_P/V_S cross-plots of all models (Models 0–5) and (b) V_P versus V_S cross-plot of all models.

the conjugate gradient formalism (Mora, 1987, 1988). The gradients estimated with respect to the Lamé constant set are then converted to the gradient set for the other elastic parameter set. The model represented by each parameter set is updated at each iteration step. Three elastic parameter sets are chosen to examine the inversion accuracy:

- Density ρ, V_P, and V_S (V_P V_S mode)
- Density ρ, P-impedance I_P, and Poisson's ratio σ (I_P Poisson mode)
- Density ρ, P-impedance I_P, and S-impedance I_S (I_P I_S mode)

These parameterisations are mathematically equivalent, but it is not self-evident that they converge to an identical result in non-linear wavefield inversion, as the minimum search tracks are not identical among them. The gradient of the misfit function is an element of 1-form or a dual of the model space. If G represents the linear operator between linear spaces, its transpose G^T is a linear operator between dual spaces (e.g. Tarantola, 1987). Taking the first order approximation of the transformation operator, the formulae for gradient transformation between these parameter sets are:

$$\begin{pmatrix} \delta\hat{V}_P \\ \delta\hat{V}_S \\ \delta\hat{\rho} \end{pmatrix} = \begin{pmatrix} 2\rho V_P & 0 & 0 \\ -4\rho V_S & 2\rho V_S & 0 \\ V_P^2 - 2V_S^2 & V_S^2 & 1 \end{pmatrix} \begin{pmatrix} \delta\hat{\lambda} \\ \delta\hat{\mu} \\ \delta\hat{\rho} \end{pmatrix} \tag{4}$$

where $\delta\hat{V}_P$, $\delta\hat{V}_S$, $\delta\hat{\rho}$ and $\delta\hat{\lambda}$, $\delta\hat{\mu}$, $\delta\hat{\rho}$ are the gradients with respect to elastic parameters V_P, V_S, ρ and λ, μ, ρ respectively.

$$\begin{pmatrix} \delta\hat{I}_P \\ \delta\hat{\sigma} \\ \delta\hat{\rho} \end{pmatrix} = \begin{pmatrix} \dfrac{2\sigma I_P}{\rho(1-\sigma)} & \dfrac{2I_P(1-2\sigma)}{\rho(1-\sigma)} & 0 \\ \dfrac{-I_P^2}{2\rho(1-\sigma)^2} & \dfrac{2I_P^2}{\rho(1-\sigma)^2} & 0 \\ \dfrac{-\sigma I_P^2}{\rho^2(1-\sigma)} & \dfrac{-I_P^2(1-2\sigma)}{2\rho^2(1-\sigma)} & 1 \end{pmatrix} \begin{pmatrix} \delta\hat{\lambda} \\ \delta\hat{\mu} \\ \delta\hat{\rho} \end{pmatrix} \tag{5}$$

where $\delta\hat{I}_P$, $\delta\hat{I}_S$, $\delta\hat{\rho}$ are the gradients with respect to elastic parameters I_P, σ, ρ respectively.

$$\begin{pmatrix} \delta\hat{I}_P \\ \delta\hat{I}_S \\ \delta\hat{\rho} \end{pmatrix} = \begin{pmatrix} 2I_P/\rho & 0 & 0 \\ -4I_S/\rho & 2I_S/\rho & 0 \\ (2I_S^2 - I_P^2)/\rho^2 & -I_P^2/\rho^2 & 1 \end{pmatrix} \begin{pmatrix} \delta\hat{\lambda} \\ \delta\hat{\mu} \\ \delta\hat{\rho} \end{pmatrix} \tag{6}$$

where $\delta\hat{I}_P$, $\delta\hat{I}_S$, $\delta\hat{\rho}$ are the gradients with respect to elastic parameters I_P, I_S, ρ respectively.

In order to examine the computational accuracy and efficiency, the subspace method (Kennett and Williamson, 1987; Crase et al., 1990) was applied to get the optimal step length projected on each orthogonal subspace for elastic parameters. This requires additional synthetic computations, including a normal equation inversion. Currently a two-dimensional space is in use:

$$m_{n+1} = m_n + \sum_{j=1}^{k} \alpha_n^j \gamma_n^j \tag{7}$$
$$\gamma_n = -C_n \hat{g}_n$$

where $\hat{g}_n$ is the gradient vector of the misfit function with respect to all parameters, and α_n^j is the step length for the model change γ_n^j with respect to the j-th subspace at the n-th iteration step. C_n is a preconditioning operator and could be represented by the inverse Hessian matrix in the Newton method (Tarantola, 1987). After numerical tests, a 2×2 diagonal matrix for scaling the average amplitude of gradient directions was

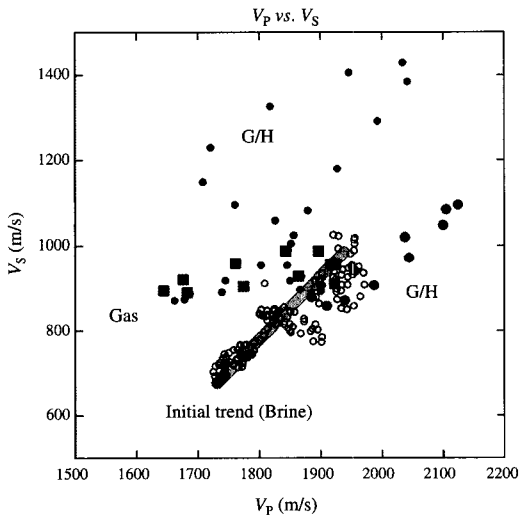

Fig. 7. V_P versus V_S cross-plot of Model 0. Brine data (open dots) are in the neighbourhood of the initial trend drawn by starting model (grey dots). Two gas hydrate zones (G/H) are illustrated by black dots. Two gas zones are illustrated by squared dots. Some black dots are seen along the same linear trend as the squared dots. These are in the interpolated data zone that is interpreted to be a newly emerged BSR in the gas hydrate zone determined by a relic BSR (double BSR hypothesis, e.g. Sakai, 2000).

used for C_n. The difference between the inversion results for the two approaches was small in the case of the simultaneous mode, although the subspace method for well correlated parameter sets is ineffective in itself (Kennett and Williamson, 1987), and also needed additional computational time. All computational results found by the preconditioned conjugate gradient method were utilised in the final error estimates.

Some computational aspects of inversion

The major problem of the inversion is how to estimate the longer wavelength velocity model (Mora, 1987, 1988, 1989). Some researchers tried to retrieve only the short wavelength variations in elastic parameters (e.g. Crase et al., 1990). But the idea of retrieving longer wavelengths was born in earlier research into acoustic inversion, (see, for instance, Kolb et al., 1986, or Pica et al., 1990). The local search method is likely to converge to local minima close to the starting model and not to the true model, if the perturbation of the starting model from the true model is large. I heuristically applied a method in my recent studies, which I have tentatively called the frequency-cascade scheme, to evaluate the full wavelength elastic-wave velocity of several two-dimensional geological models (Sakai, 2002, 2003). The frequency-cascade scheme was found to be effective in resolving this problem. If it is realised in a multi-grid formulation, starting at the lowest source frequency and increasing source frequency as the grid size is reduced according to the stability criterion, there is a computational benefit.

$$\Delta t < 0.606\frac{\Delta}{V_{\max}} \tag{8}$$

where Δt, Δ, and $V_{\max}$ are time grid, space grid, and maximum V_P values. Cascaded frequencies can be determined from the grid size series, for example by halving the spatial size and doubling the frequency. In the current study, I changed the source frequencies alone in actual synthetic computations as the data volume was not so large. As an efficient searching method, Bunks et al. (1995) had already applied the multi-grid method to the acoustic inversion problem, which decomposes the problem into scales in the same manner as the current method.

In an acoustic survey of a single reflector, cascaded frequencies represented by single frequency sinusoidal sources are estimated by a simple relation defined by the maximum receiver offset and reflector depth in the frequency-domain inversion approach (Sirgue and Pratt, 2001). It is shown that the number of cascaded frequencies is reduced if the maximum offset increases. This is an interesting approach that gives a guide to frequency selection, but in elastic surveys over complex structures, we need a trial and error approach for optimal frequency selection (Sirgue and Pratt, 2001). Note that computational efficiency is higher in acoustic inversion by the frequency-domain approach than the current time–space domain approach, although memory requirements are larger in the frequency-domain approach. Elastic inversion by the frequency domain approach has not been well implemented with real or synthetic data.

In elastic wavefield inversion, elastic parameters such as V_P and V_S can be estimated by several approaches. In some cases, for example, where P-wave logging data exists, the P-wave velocity model structure may be well constrained in advance, and the S-wave velocity alone is estimated by inversion with fixed P-wave velocity, and vice versa, which I call constrained mode. Alternating mode or relaxation mode means that first V_P is updated with V_S fixed, and subsequently V_S is updated with V_P fixed, at each iteration step. Simultaneous mode means that the P- and S-wave velocities are estimated simultaneously at each iteration step of the inversion. Computational experiments show that simultaneous mode is more efficient and accurate than constrained mode or alternate mode (Sakai, 2002, 2003). There are other strategies that combine several approaches, and so might be called hybrid mode. One such example is to increase the maximum receiver offset in inversion, i.e. estimating shorter wavelength P-wave velocity or P-impedance variations by short-offset inversion, and longer wavelength P- and S-wave velocity or Poisson's ratio variations by subsequent longer offset inversion (e.g. Igel et al., 1996), tentatively called offset-based hybrid mode. For efficiency and accuracy in inversion, a frequency-cascade scheme with the simultaneous mode approach is better than others, as well as being simple to implement regardless of model complexity.

Another problem is how to construct starting models to realise a full wavelength velocity model. Mora (1989) gave insight into this problem for the case of acoustic inversion, by demonstrating that the inversion is equivalent to simultaneously doing migration and reflection tomography. He provided a recipe to add a transmission or tomographic component in acoustic reflection surveys by adding a deepest reflector below the target zone, to generate transmission waves as a single pass of the deep reflection. A starting model of linear P- and S-wave velocity trends as a function of depth is chosen to realise transmission or tomographic components in the inversion of the elastic reflection survey in the same manner as the additional deepest reflector. This corresponds to generating refracted or diving waves for longer offsets. The longest wavelength velocity model is represented by such a linear velocity trend as a function of depth to stabilise the inversion for all wavelengths. Taking such a simple starting model as a rule of thumb proves to be very effective in combination with the frequency-cascade scheme (Sakai, 2002, 2003). Another physical reason to take a linear velocity trend as a function of depth is that we have a good chance to estimate a proper V_P versus V_S relation in advance, although this initial trend itself will be updated by the inversion.

Numerical test

1D model building

In the numerical tests, layered elastic models are adopted for computational efficiency. Model 0 is constructed from log data from the gas hydrate well in the Nankai Trough where, in order to reduce the number of grids for computational efficiency, water depth is set to 110 m. This consequently makes water-bottom multiples prominent compared with the original geometry. To incorporate possible elastic parameter fluctuations in depth and consider the statistics of errors of the inversion in the broad parameter domain, I constructed additional models in the following manner. Taking perturbations δV_P and δV_S from linear P- and S-wave velocity trends as a function of depth, and initial velocity trends $V_{P,i}$ and $V_{S,i}$, new V_P and V_S models are generated as follows:

$$\begin{array}{lll}
\text{Model 0} & V_P = \delta V_P + V_{P,i} & V_S = \delta V_S + V_{S,i} \\
\text{Model 1} & V_P = \delta V_S + V_{P,i} & V_S = \delta V_P + V_{S,i} \\
\text{Model 2} & V_P = -\delta V_S + V_{P,i} & V_S = -\delta V_P + V_{S,i} \\
\text{Model 3} & V_P = \delta V_S + V_{P,i} & V_S = -\delta V_P + V_{S,i} \\
\text{Model 4} & V_P = \delta V_P + V_{P,i} & V_S = \delta V_P + V_{S,i} \\
\text{Model 5} & V_P = \delta V_P + V_{P,i} & V_S = -\delta V_P + V_{S,i}
\end{array} \tag{9}$$

Model 0 is shown in Figure 5 and other models are shown in the V_P versus V_S and V_P versus V_P/V_S cross-plots in Figure 6.

Initial velocity perturbations, defined by $\delta V_P/V_P$ and $\delta V_S/V_S$, of V_P and V_S for each model reach ~50%. Note that a cross-plot of V_P and V_S for Model 0, shown in Figure 7, depicts two obliquely intersecting trends, a brine- and a gas-bearing zone. Scattered black filled dots surrounding these two trends in Figure 7 depict gas hydrates.

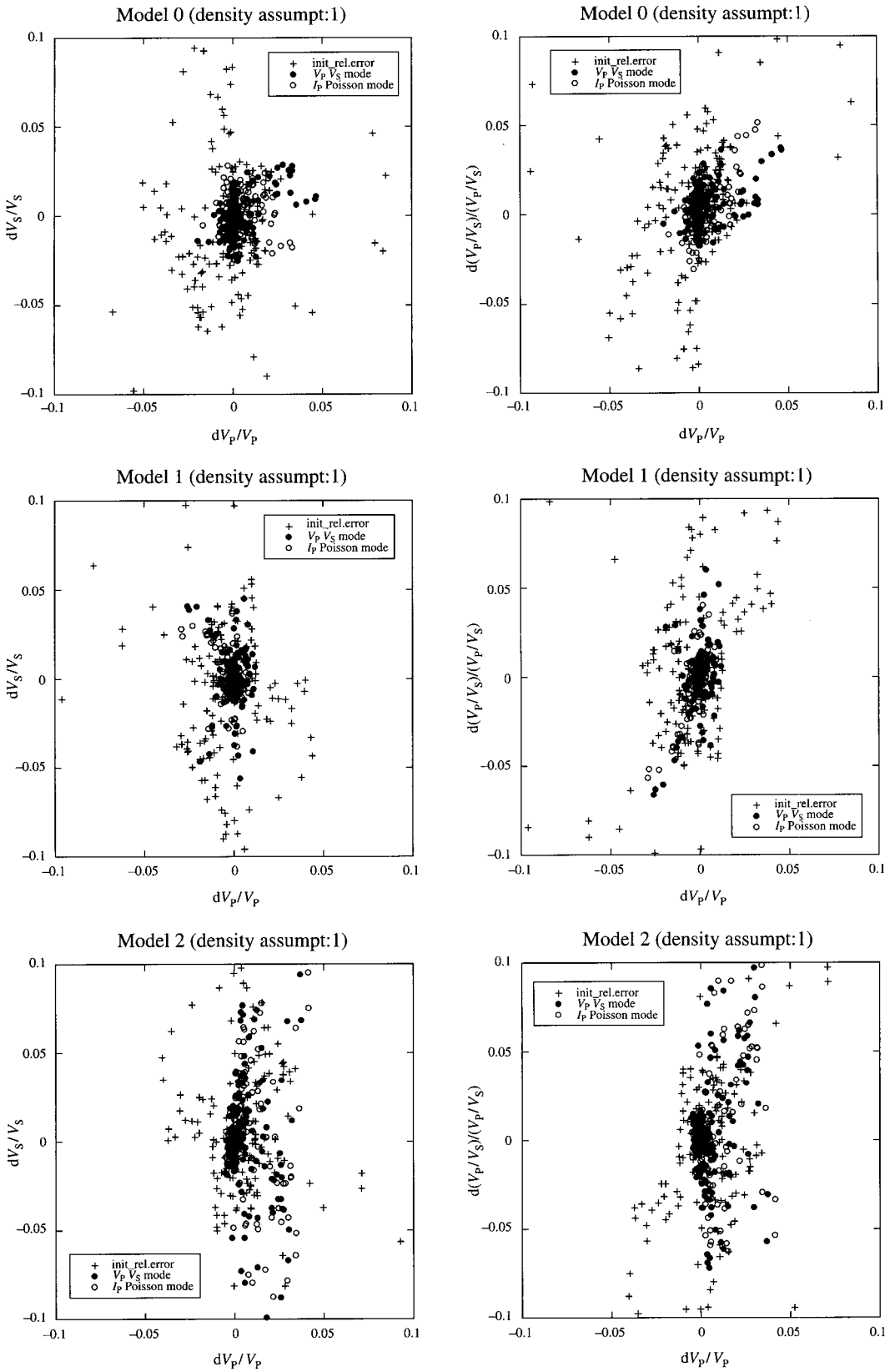

Fig. 8. Cross-plots of the relative errors V_P, V_S, and V_P/V_S in dV_P/V_P versus dV_S/dV_S and dV_P/V_P versus $d(V_P/V_P)/d(V_P/V_S)$ for V_P V_S mode and I_P Poisson mode inversion with the first density update assumption for six models (only value ranges between –0.1 and 0.1 are illustrated). Initial relative errors are shown by crosses, inverted relative errors for V_P V_S mode are black dots, and those for I_P Poisson mode are black open circles.

Density assumptions

In the current inversion method, density is assumed to be a function of P-wave velocity according to the combined relations of Gardner et al. (1974) and Hamilton (1978). Inversion of the elastic parameters is done with the following schemes for density updates. Density is not estimated by the inversion, so to know the effects of density in the current inversion results, I assumed three versions of the density update algorithm, and compared the inversion accuracy in three modes.

1. $\rho^i = \rho(V_P^i)$ at the start of the i-th inversion step, where ρ^i and V_P^i are density and P-wave velocity at the start of the

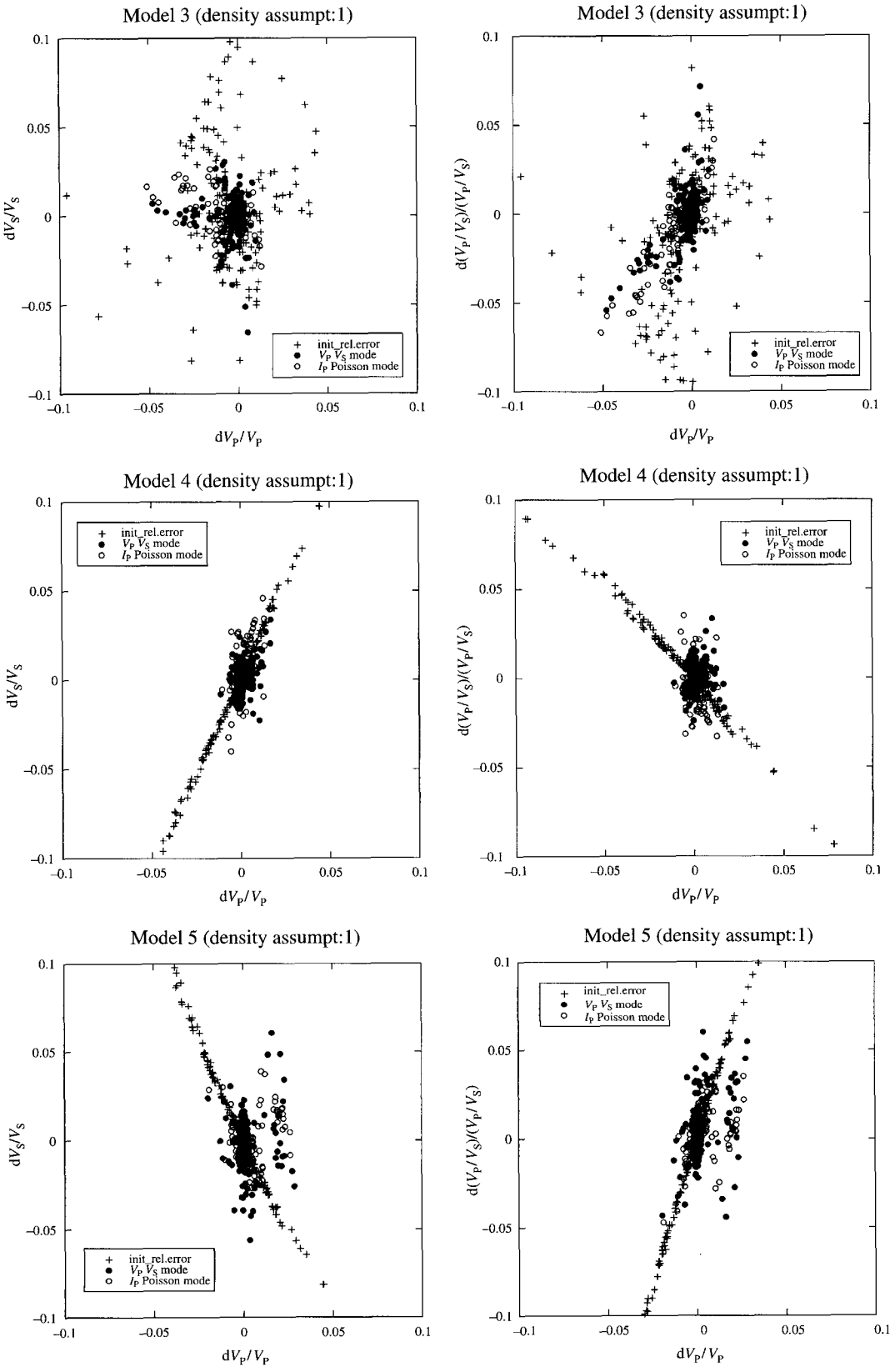

Fig. 8. (continued)

i-th step. Density is then updated from the inverted V_P for the next step.

2. $\rho^i = \rho(V_P^0)$ at the i-th inversion step where V_P^0 is the P-wave velocity at the initial step, and ρ^i is density at the i-th step. Density is constant, equal to the initial value computed from the initial P-wave velocity.
3. $\rho^i = Q\rho(V_P^i)$ where Q is the quotient of updated and current density values as a function of P-wave velocity. Q is chosen from 0.8, 0.9, 1.1, 1.2, 1.3, and 2.0 as inversion cases.

In V_P V_S mode and I_P Poisson mode, density is updated by all three density assumptions with updates of V_P and V_S. In I_P I_S mode, density is kept at the initial value and the elastic parameters are inverted under the second assumption.

I use the following cases to compare the inversion accuracy in the relative error of V_P, V_S, and V_P/V_S:

- Models for the V_P V_S mode and I_P Poisson mode with the first density update assumption;
- Models for the V_P V_S mode, I_P Poisson mode, and I_P I_S mode with the second density update assumption;
- A model for the V_P V_S mode and I_P Poisson mode with the third density update assumption.

To display the statistical error distribution, relative errors are illustrated by histograms classed by Akaike's Information Criterion (AIC, see Appendix) in addition to cross-plots of relative errors.

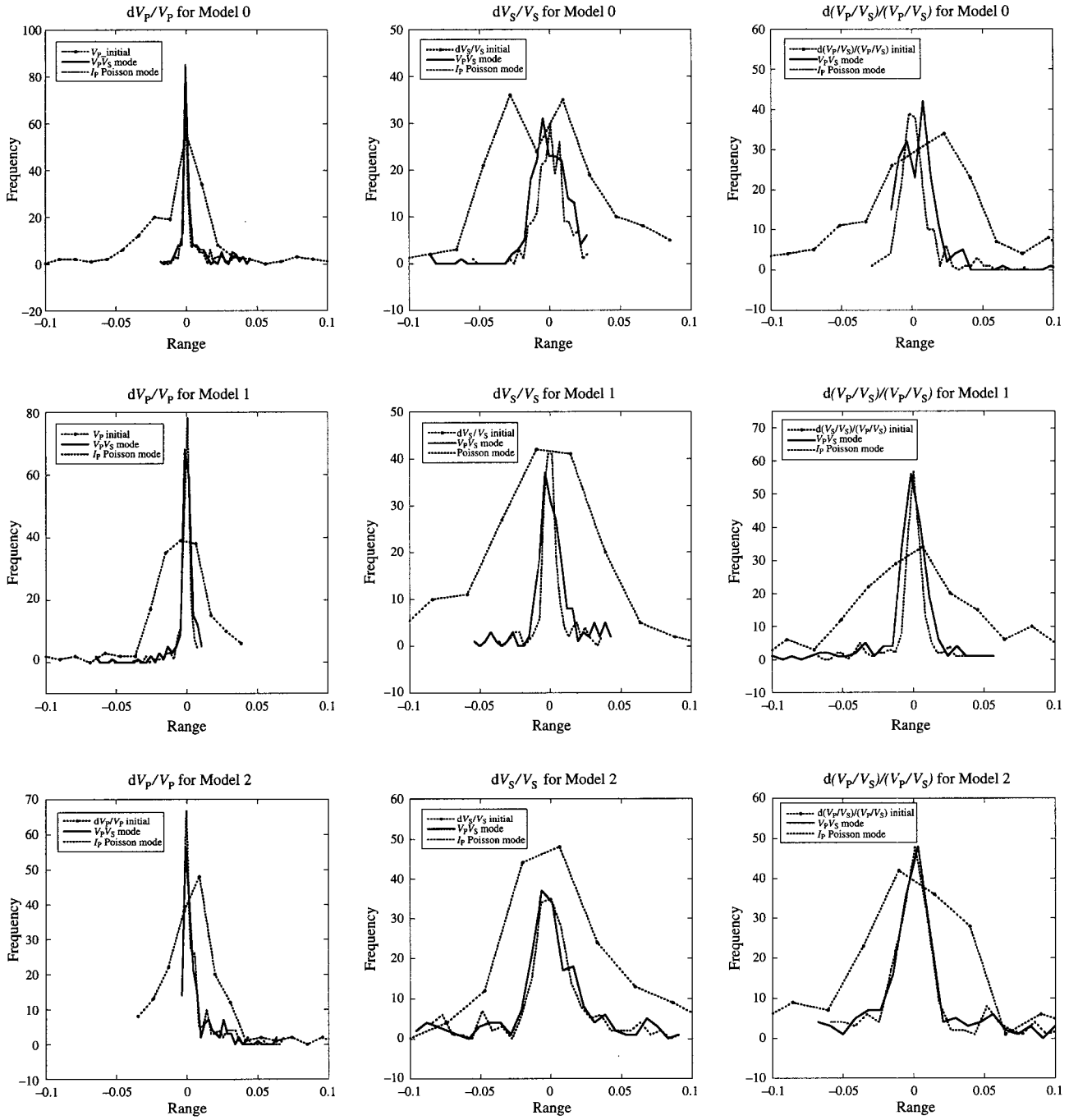

Fig. 9. Histograms of the relative errors V_P, V_S, and V_P/V_S of V_P V_S mode and I_P Poisson mode inversion of the first density assumption (black curves and black dotted curves respectively) for six models, with the starting model shown by black dotted curves with markers. Histogram classes are determined by AIC for the multinomial distribution of relative errors and are only illustrated between –0.1 and 0.1.

Numerical results for 1D models

The grid size is kept at 1 m for all frequency steps, and the number of model depth grids is 298. The maximum number of receiver channels is 100 at a 10 m receiver interval, giving a 1000 m maximum offset. The ratio of the deepest depth to maximum offset is ~0.3. The source function is assumed to be a Gaussian function, with a specified dominant frequency. Source and receivers are deployed at 1.5 m depth below the free surface. The frequency-cascade scheme is now designed with the dominant frequencies 20, 40, and 80 Hz, with 40 iterations.

The relative error of V_P and V_S is defined as $(V_{inv} - V_{true})/V_{true}$ where V_{inv} is the inverted velocity and V_{true} is the given velocity model for V_P and V_S. Relative error of V_P/V_S is defined as $[(V_{P,inv}/V_{S,inv}) - (V_{P,true}/V_{S,true})] / (V_{P,true}/V_{S,true})$, where $V_{P,inv}$, $V_{S,inv}$, $V_{P,true}$, and $V_{S,true}$ are the inverted and given models for V_P and V_S.

Inversion results under the density update assumptions

In Figure 8, the cross-plots of relative errors V_P, V_S and V_P/V_S in dV_P/V_P versus dV_S/V_S and dV_P/V_P versus $d(V_P/V_S)/(V_P/V_S)$ of the initial and inverted models are illustrated for comparison between V_P V_S mode and I_P Poisson mode for Models 0–5, with inversion under the first density update assumption in the value ranges between –0.1 and 0.1 (although the absolute values of relative errors of the initial model are larger than 0.1). In Figure 9, the histograms of relative errors of the initial and inverted models are illustrated in the value ranges between

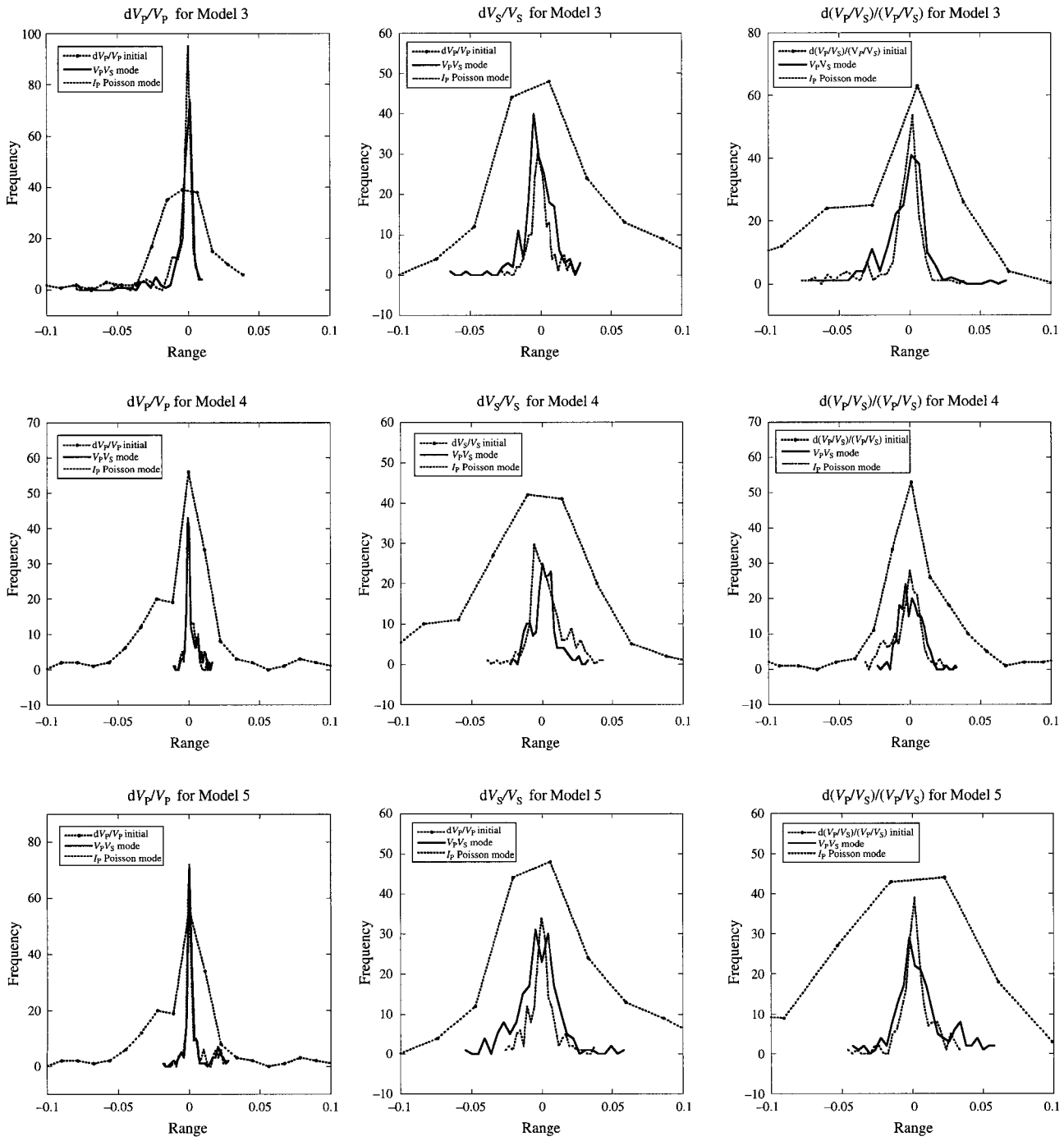

Fig. 9. (continued)

–0.1 and 0.1 for comparison between V_P V_S mode and I_P Poisson mode for all Models, with inversion under the first density assumption. Generally the accuracy of P-wave velocity inversion is excellent over all models as represented by relative errors. The inversion results do not show noticeable systematic differences in the statistics of relative errors between V_P V_S mode and I_P Poisson mode for the models used. Relative errors of V_P, V_S and V_P/V_S are highly correlated or anti-correlated in Model 4 and Model 5, but even in those cases the inversion was successfully completed in high accuracies.

In Figure 10, the histograms of relative errors of the initial and inverted models are illustrated in the value ranges between –0.1 and 0.1 for comparison between V_P V_S mode and I_P Poisson mode, for all models with inversion under the second density update assumption. Under this assumption, there are no systematic differences in the statistics of relative errors between V_P V_S mode and I_P Poisson mode. The relative errors in V_S and V_P/V_S in Model 0 are slightly larger than in the other models. Relative errors in depths of Model 0 do not have any correlation with the depth discrepancy between starting and true models, although this model has the largest V_S discrepancy, but there is a discrepancy in the trend of longer wavelengths in depth.

The accuracy of V_P remains comparable under both density update assumptions, but the relative errors of V_S and V_P/V_S under the second assumption are smaller than those under the first assumption. This is because density is kept equal to the initial density model during every inversion step.

In Figure 11, the inverted model and the true model are illustrated in a cross-plot of V_P versus V_S for V_P V_S mode as open circles and I_P Poisson mode as black dots, for the

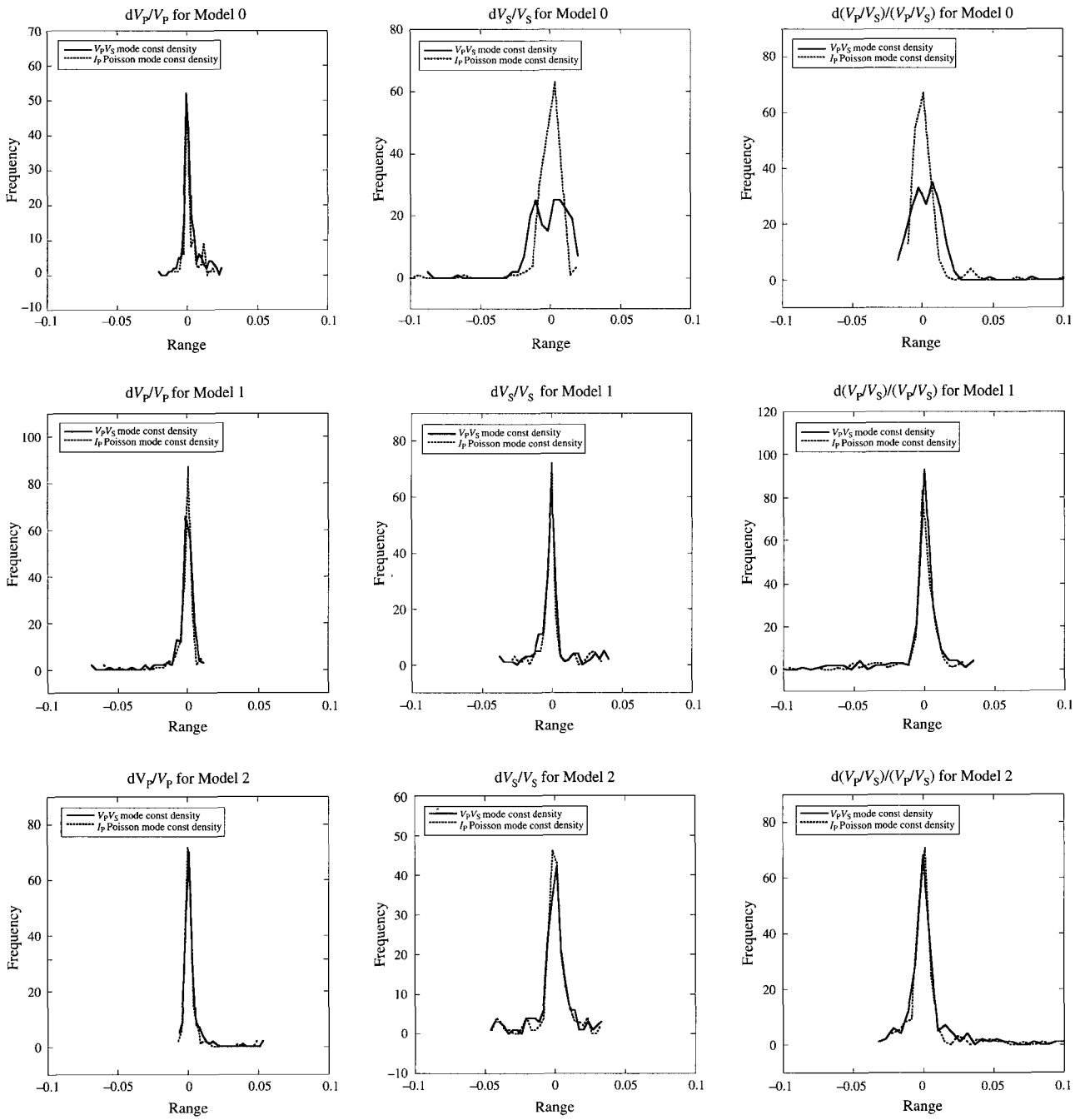

Fig. 10. Histograms of the relative errors V_P, V_S, and V_P/V_S for V_P V_S mode and I_P Poisson mode inversion with the second density assumption (black curves and black dotted curves respectively) for six models. Histogram classes are determined by AIC for the multinomial distribution of relative errors and are only illustrated between –0.1 and 0.1.

case of Model 0 with the third density update assumption with quotient 2.0 (taken as an extreme case of the third density update assumptions). True model data are illustrated as small open circles. The gas-bearing and gas hydrate zone is well inverted for both modes (refer to Figure 7) even though the starting model has significant discrepancies from the true model. In Figure 12 are shown histograms of relative errors of V_P, V_S, and V_P/V_S for V_P V_S mode and I_P Poisson mode for quotients 0.8 and 2.0. Note that there is no conspicuous difference between quotient 0.8 and 2.0 for these modes. This implies that the sensitivity to density is small for our model geometry although the ratio of the deepest depth to maximum offset is as small as 0.3. The experiment of Dębski and Tarantola (1995) was done with a ratio of 0.44, which is larger than the current one. According to the current inversion results, if there were density effects, they would actually appear at larger offsets than the current ones. This character can be regarded as a favourable point because the wavefield inversion is robust in density values, therefore we do not have to define accurate density relations. On the other hand, it would be considered unfavourable as the inversion is insensitive to the density values, meaning that we cannot easily estimate accurate density values.

Effects of noise

In real world reflection surveys, noise is inevitable. To examine such effects, Gaussian noise is added to the synthetic reflection data at signal-to-noise levels of 200, 100, 50, and 25. In Figure 13, synthetic shot records are shown for signal-to-noise ratio (S/N) of 25 and noise-free conditions. In Figure 14, the inverted models are displayed for comparison between V_P V_S

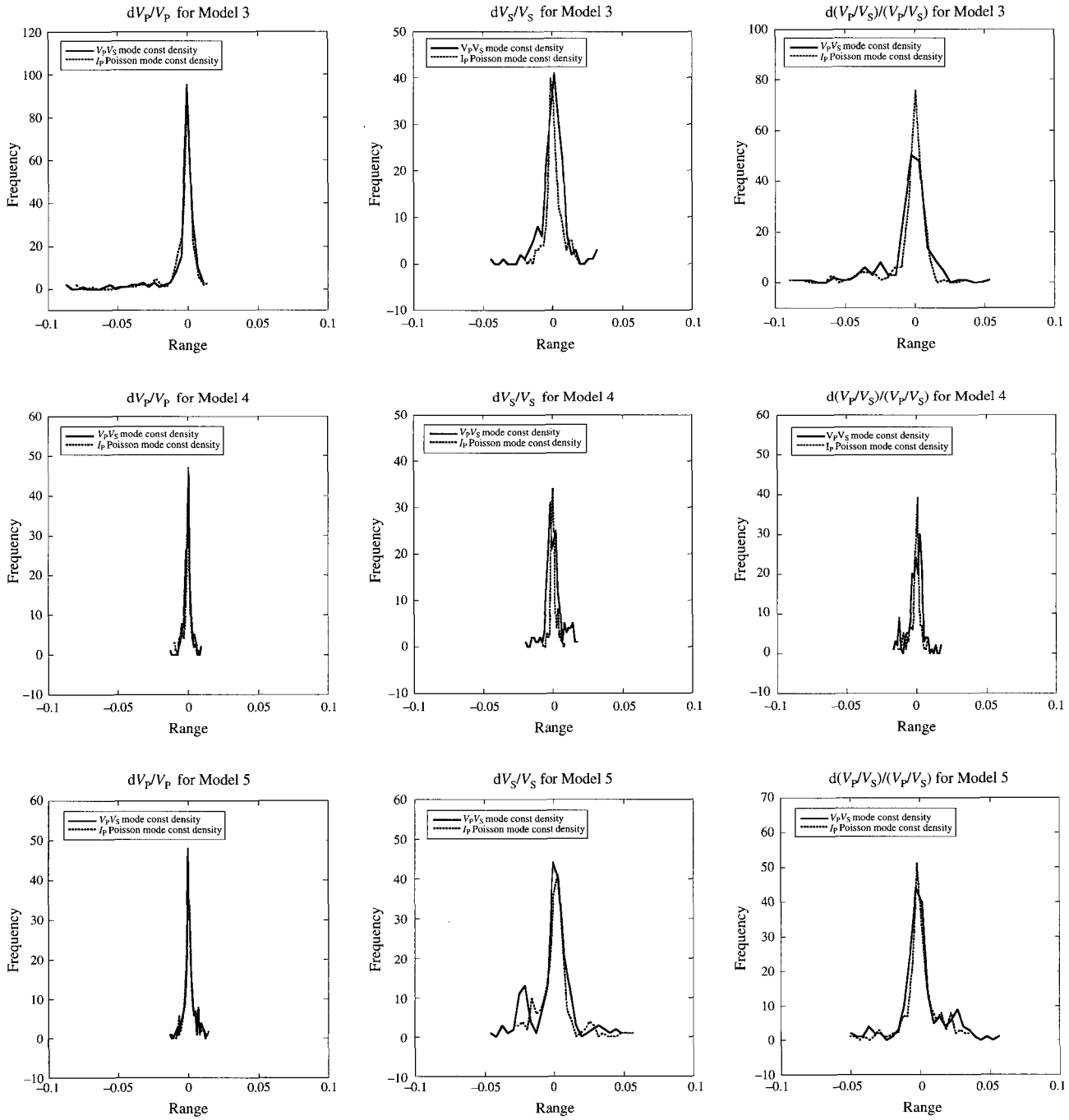

Fig. 10. (continued)

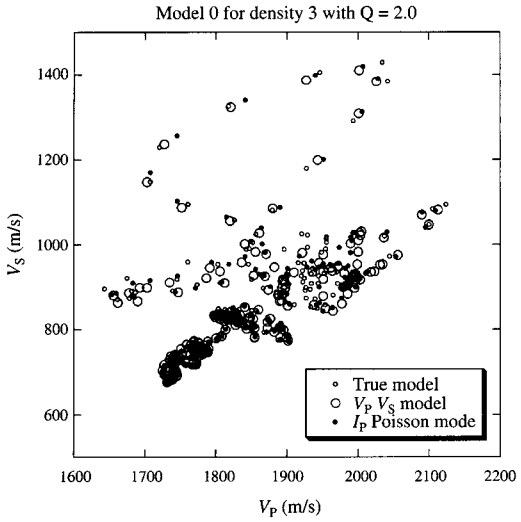

Fig. 11. An example of an inversion result for Model 0 by V_P V_S mode indicated by black open circles and I_P Poisson mode indicated by black dots. The true model is illustrated by small black open circles. Inversion is done under the third density update assumption with quotient 2.0.

mode and I_P Poisson mode, for S/N of 25, Model 0, and the first density update assumption. The accuracy of V_P is in the acceptable range compared with noise-free cases for both V_P V_S mode and I_P Poisson mode. The accuracy of V_S is worse in the depth range where velocity fluctuation is moderate than in the depth range of larger velocity fluctuation. As an extreme case of the S/N cases examined, Figure 15 shows marginal distributions of relative errors of V_P, V_S and V_P/V_S for all models with S/N of 25 under the first density assumption for V_P V_S mode and I_P Poisson mode. For other S/N values, there are no specific differences in relative errors between V_P V_S mode and I_P Poisson mode in the inversion for all six models.

Effects of maximum offset distance

The accuracy of the elastic-wave velocity in the deeper zone is related to the maximum offset range. To examine its effect in inversion, the model was inverted after increasing the number of receiver channels from 100 to 160 (1 to 1.6 km offset distance). In this case, the ratio of deepest depth to maximum offset is approx. 0.19. With this receiver geometry, deeper V_P values are inverted more accurately than the model with the originally defined receiver geometry. In Figures 16 and 17, the inverted model

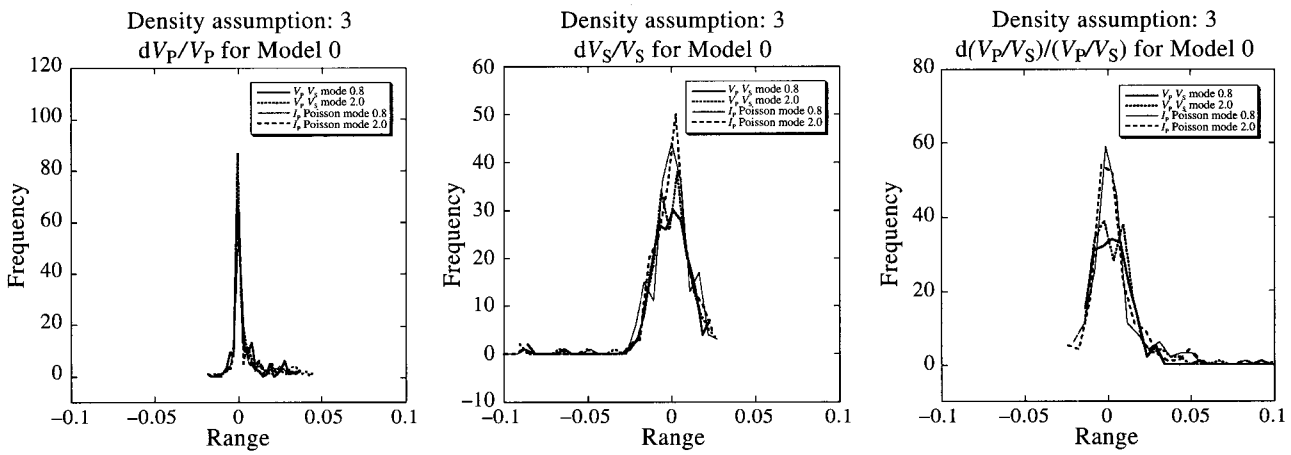

Fig. 12. Histograms of the relative errors V_P, V_S, and V_P/V_S for V_P V_S mode inversion with the third density update assumption of quotient 0.8 and 2.0 (black and dotted curves respectively), and I_P Poisson mode inversion with the third density assumption of quotient 0.8 and 2.0 (thin black and dotted curves respectively) for Model 0. Histogram classes are determined by AIC for the multinomial distribution of relative errors.

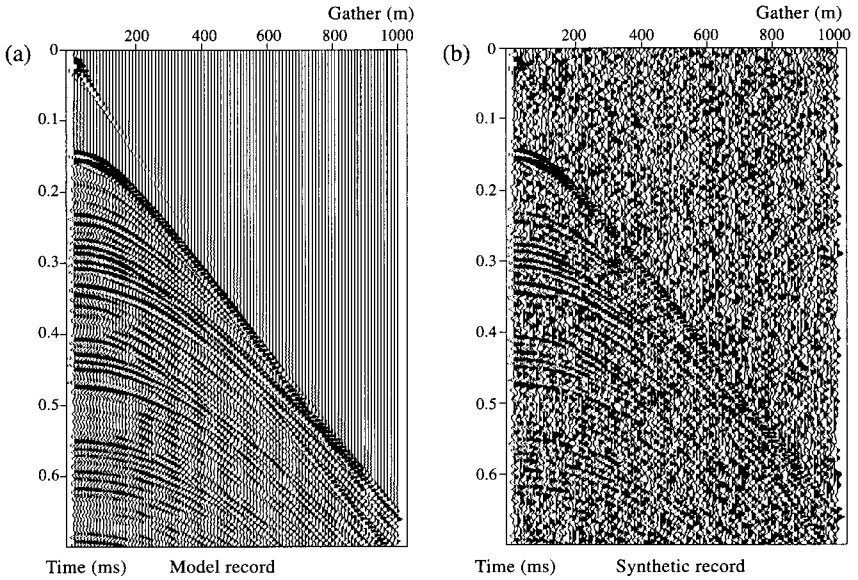

Fig. 13. (a) Synthetic noise-free shot record. (b) Synthetic shot record for Model 0 with S/N = 25.

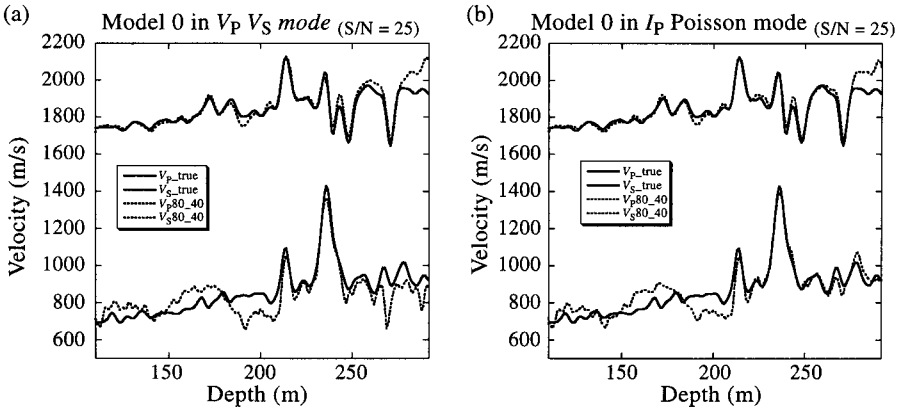

Fig. 14. True and inverted velocity models for a synthetic shot record with S/N = 25, for Model 0 under the first density update assumption in (a) the V_P V_S mode and (b) the I_P Poisson mode (thick curves: true V_P and V_S model, dotted curves: inverted V_P and V_S model).

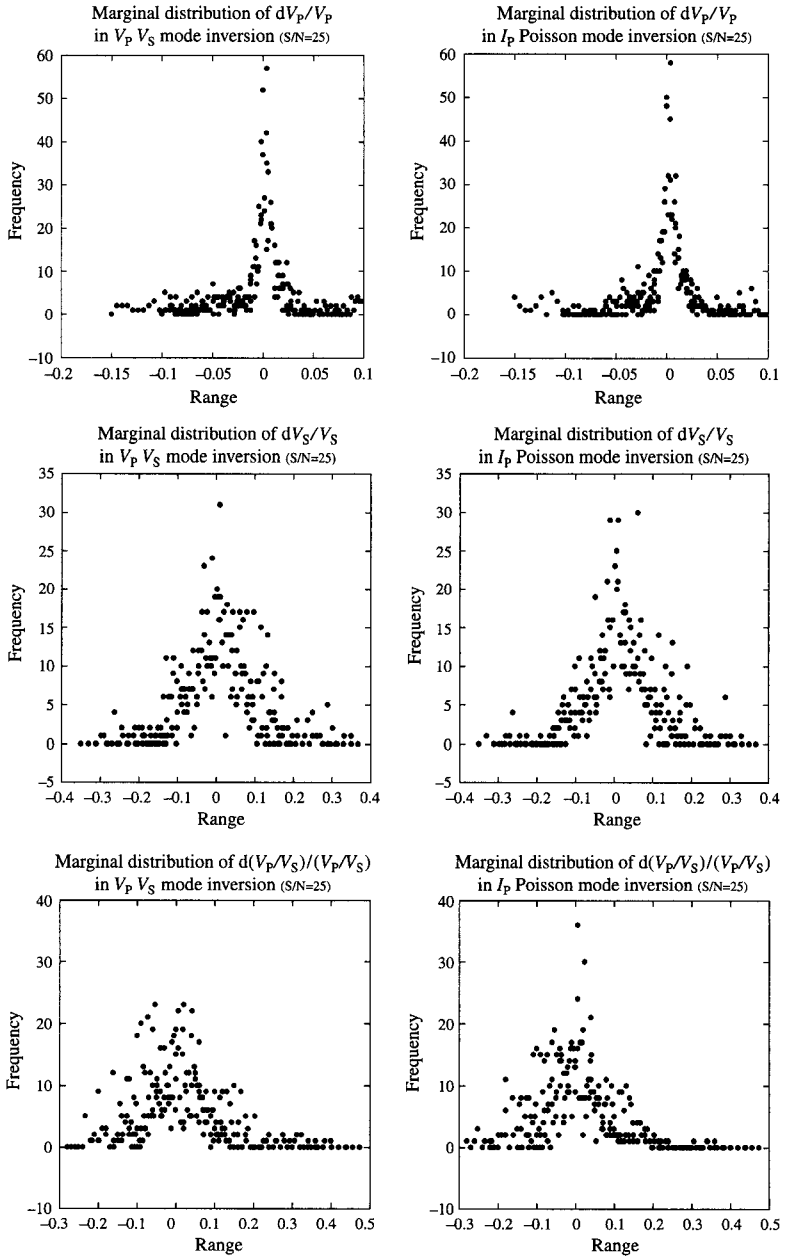

Fig. 15. Marginal distribution of relative errors of V_P, V_S, and V_P/V_S for all six models with S/N = 25 using the first density update assumption for the V_P V_S mode and the I_P Poisson mode.

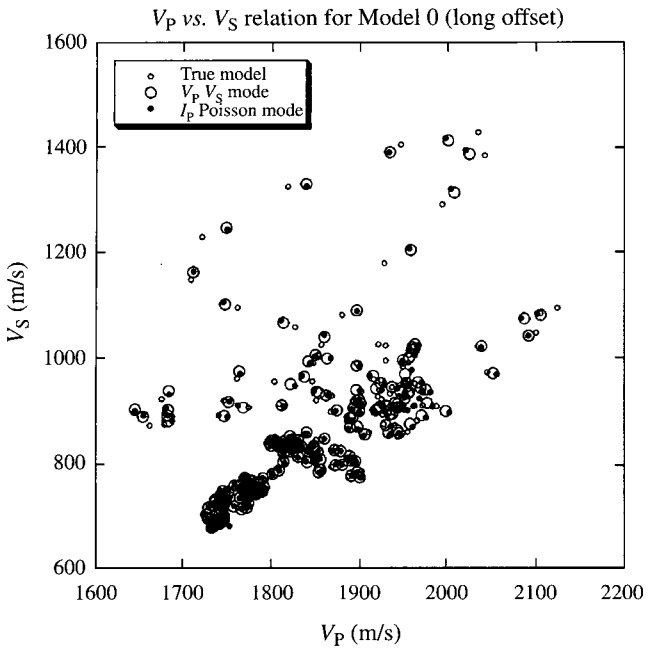

Fig. 16. An example of inversion result for Model 0 of longer offset receiver geometry (160 channels) for V_P V_S mode indicated by black open circles and I_P Poisson mode indicated by black dots. The true model is illustrated by small black open circles. Inversion is done under the first density assumption.

with the true model of longer offset geometry are illustrated in cross-plots of V_P versus V_S and histograms of relative errors of V_P, V_S and V_P/V_S for V_P V_S mode and I_P Poisson mode in the case of Model 0, as an example, under the first density update assumption. Generally, if the maximum offset is larger than that originally defined, the inversion accuracy of the elastic-wave velocity at the deepest reflectors of the models would be improved over the current estimates, though the similarity of error distributions in elastic parameter sets will not be much affected under the current geometry.

Numerical experiment for a 2D model

Next I examined a 2D model for three parameter sets in the wavefield inversion scheme. It is an elastic-wave velocity model of rock intrusion, with lower P-wave velocity in the upper layer and higher P-wave velocity in the lower part in the medium, and laterally invariant linear velocity trends with depth. To simulate broad elastic parameter fluctuations in the model, the rock intrusion has a depth-shifted P- and S-wave velocity anomaly distribution illustrated in Figure 18 (Sakai, 2002). In Figure 19 are illustrated a 1D elastic-wave velocity model profile at the centre of the rock intrusion. The grid size is kept at 20 m for all frequency steps and the number of model depth grids is 101. The maximum number of receiver channels is 80, at a 100 m receiver interval, with the nearest offset 300 m giving 8200 m maximum offset. The ratio of the deepest depth of the anomaly to maximum offset is ~0.2. The source function is assumed to be a Gaussian function with a specified dominant frequency. Source and receivers are deployed at 10 m depth below the free surface. Shot interval is 200 m. The frequency-cascade scheme, coded for multi-shots with the OpenMP parallel programming platform (www.openmp.org), is now implemented with dominant frequencies 3, 6, and 12 Hz, with 40 iterations respectively. The density is updated by the first density assumption in the V_P V_S mode and I_P Poisson mode, and by the second density assumption for the I_P I_S mode.

In Figure 20 are shown the histograms of relative errors of V_P, V_S and V_P/V_S in V_P V_S mode, I_P Poisson mode, and I_P I_S mode respectively. Initial relative errors are overlaid in these histograms. Relative errors in the inversion results are within the absolute ranges of 0.05 in all modes. Relative error statistics are almost identical among the three modes, and have the same features as in the 1D models.

Discussion and conclusions

It is standard practice in reflection seismology to decouple the longer and shorter wavelength reflection data, say, by traveltime analysis and reflectivity analysis. I have examined information for several parameter sets across a wavelength range that was not covered in full by Dębski and Tarantola (1995). Taking a different approach for the discussion of the maximum information of elastic parameter sets, the present study directly estimates the full wavefield inversion accuracy in terms of the relative errors of V_P, V_S, and V_P/V_S in elastic parameter sets V_P V_S mode, I_P Poisson mode, and I_P I_S mode for several models. From the accuracy of inversion of the full wavelength data for the several models used, it can be concluded that there is no specific difference between the V_P V_S mode and the I_P Poisson mode in terms of inversion error distributions. The same conclusion is expected for the I_P I_S mode, although the number of inversion trials are fewer than other sets in the current study.

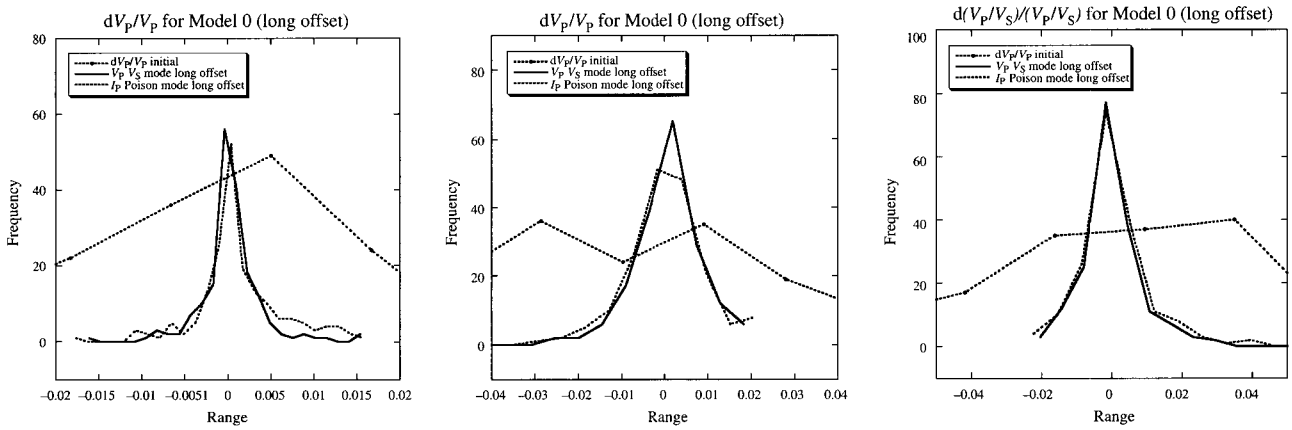

Fig. 17. Histograms of the relative errors V_P, V_S, and V_P/V_S of part of the initial models (black dotted curves with markers), V_P V_S mode inversion (black curves), and I_P Poisson mode inversion (black dotted curves). Inversion is done under the first density assumption. Histogram classes are determined by AIC for the multinomial distribution of relative errors.

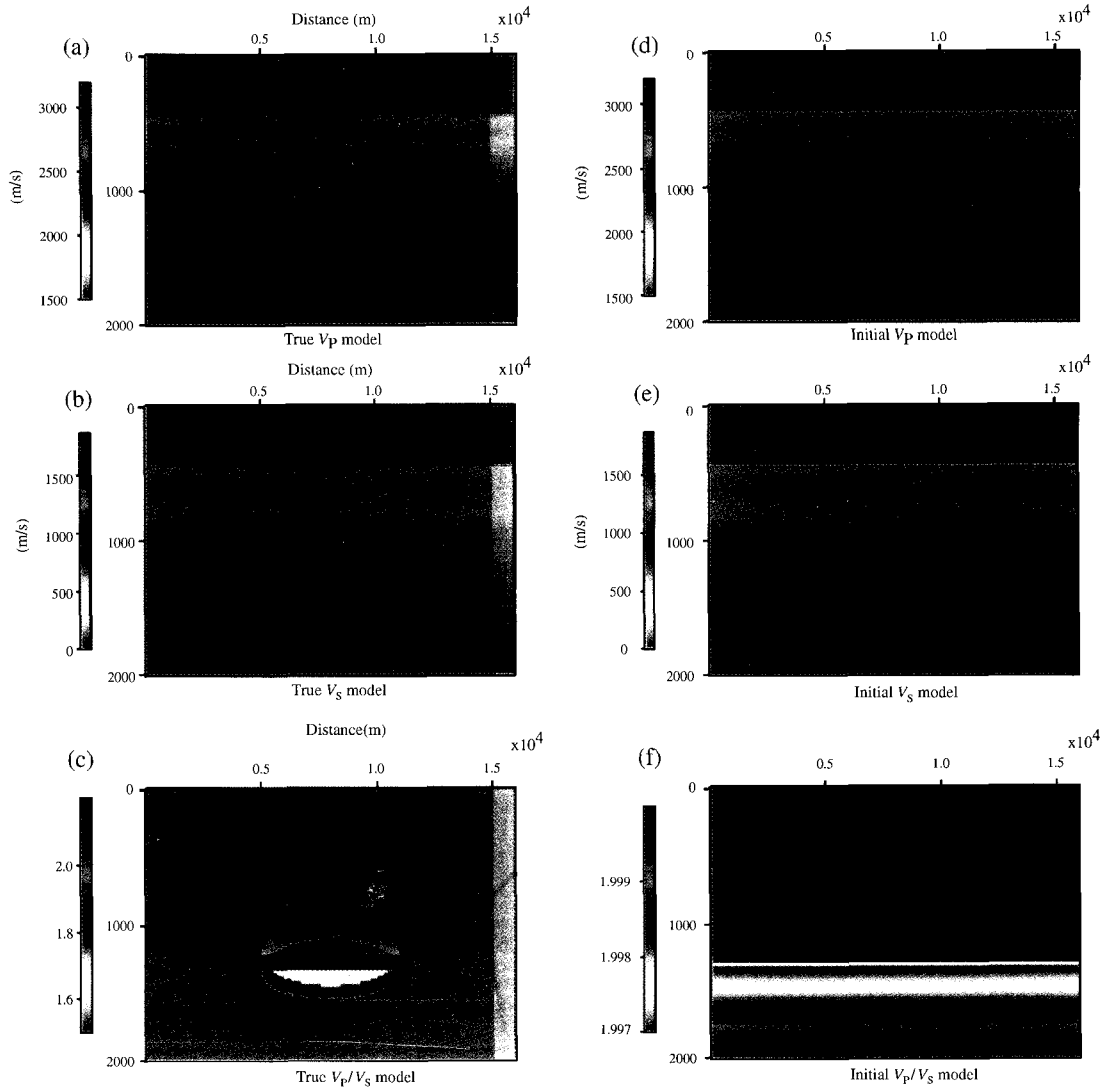

Fig. 18. 2D elastic velocity model of a rock intrusion into a medium with starting model of laterally invariant linear velocity trend in depth (a–c: V_P, V_S, and V_P/V_S for the elastic velocity model; d–f: V_P, V_S, and V_P/V_S of the starting model).

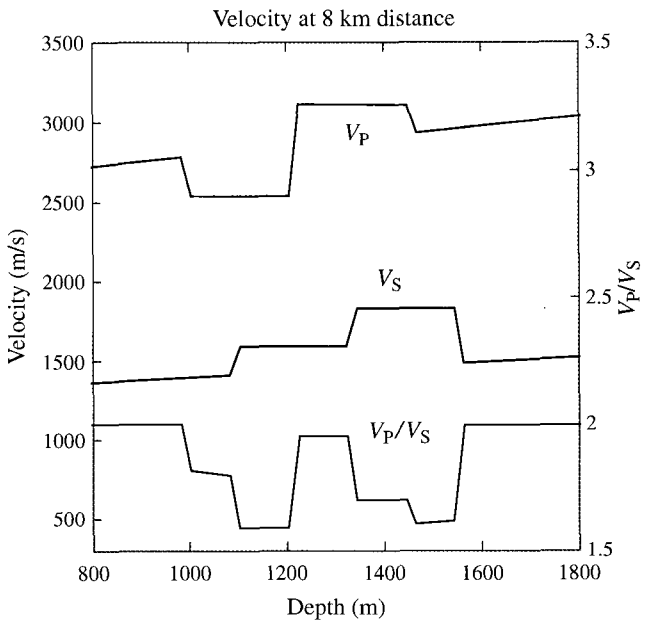

Fig. 19. 1D elastic-wave velocity model profile at the centre of the 2D rock intrusion model.

Some researchers have declined to estimate the longer wavelength velocity distributions (e.g. Crase et al., 1990), and some have adopted the I_P Poisson mode in advocating a constrained mode inversion (e.g. Igel et al., 1996). Inversion accuracy is dependent on the strategy of inversion and details of the algorithm, as well as the formulation of the elastic parameter set. In the present paper, a frequency-cascade scheme is incorporated in simultaneous mode of the inversion scheme, which leads to highly accurate inversion results for the whole range of wavelengths, although it requires extensive computer resources. Simultaneous mode inversion for all parameter sets, which was applied only to V_P V_S mode in Sakai (2002, 2003), is confirmed to be stable and efficient in the I_P Poisson mode and the I_P I_S mode, although Igel et al. (1996) and others have suggested that it is unstable in their I_P Poisson mode studies, so that they adopted an offset-based hybrid mode. It would be convenient for accurate full wavelength inversion if there were no preference among elastic parameter sets. It was important to examine the sensitivity of the density distribution in the current full wavelength inversion trials. However, for the survey geometry and the models used here, the sensitivity to density distributions proves to be very small. More study, using much longer offset data, is needed to further increase the accuracy of inversion of elastic parameters,

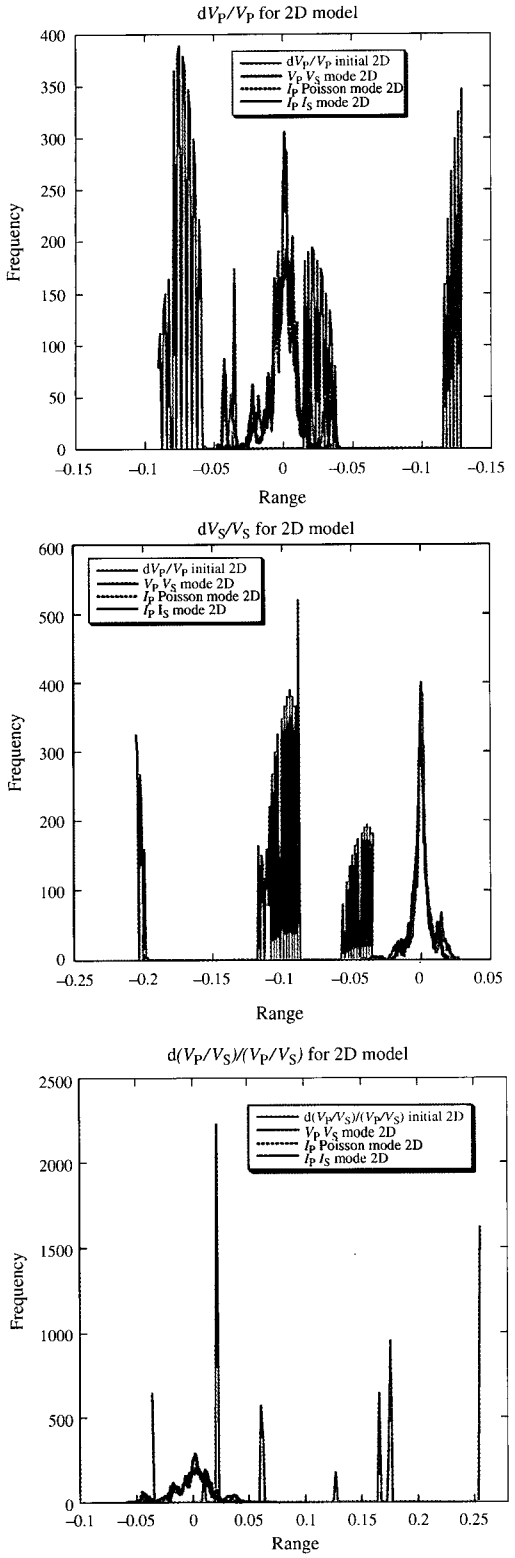

Fig. 20. Histograms of relative errors of V_P, V_S, and V_P/V_S for V_P V_S mode, I_P Poisson mode, and I_P I_S mode, shown by the purple curve, blue dotted curve, and green curve, respectively. Initial relative errors are shown by a cyan curve in these histograms. Histogram classes are determined by AIC for the multinomial distribution of relative errors.

including inversion for three parameters simultaneously, and to further discuss the maximum information in possible parameter sets.

References

Akaike, H., 1974, New look at statistical-model identification: *IEEE Transactions on Automatic Control* **19**, 716–723. doi: 10.1109/TAC.1974.1100705

Arts, R. O., Eiken, A., Chadwick, P., Zweigel, P., van der Meer, L., and Zinszner, B., 2002, Monitoring of CO2 injected at Sleipner using time lapse seismic data: *Proceedings of GHGT-6, Kyoto*, 347–352.

Bunks, C., Saleck, F. M., Zaleski, S., and Chavent, G., 1995, Multiscale seismic waveform inversion: *Geophysics* **60**, 1457–1473. doi: 10.1190/1.1443880

Claerbout, J. F., 1985, *Imaging of the Earth's Interior*: Blackwell.

Crase, E., Pica, A., Noble, M., McDonald, J., and Tarantola, A., 1990, Robust elastic nonlinear waveform inversion: Application to real data: *Geophysics* **55**, 527–538. doi: 10.1190/1.1442864

Dębski, W., and Tarantola, A., 1995, Information on elastic parameters obtained from the amplitudes of reflected waves: *Geophysics* **60**, 1426–1436. doi: 10.1190/1.1443877

Dvorkin, J., Prasad, M., Sakai, A., and Lavoie, D., 1999, Elasticity of marine sediments: Rock physics modelling: *Geophysical Research Letters* **26**, 1781–1784. doi: 10.1029/1999GL900332

Gardner, G. H. F., Gardner, L. W., and Gregory, A. R., 1974, Formation velocity and density: The diagnostic basis for stratigraphic traps: *Geophysics* **39**, 770–780. doi: 10.1190/1.1440465

Hamilton, E. L., 1978, Sound velocity-density relations in sea-floor sediments and rocks: *The Journal of the Acoustical Society of America* **63**, 366–377. doi: 10.1121/1.381747

Igel, H., Djikpesse, H., and Tarantola, A., 1996, Waveform inversion of marine reflection seismograms for P impedance and Poisson's ratio: *Geophysical Journal International* **124**, 363–371.

Kennett, B. L. N., and Williamson, P. R., 1987, Subspace methods for large scale nonlinear inversion: In Vlaar, N. J., Nolet, G., Wortel, M. J. R., and Cloetingh, S. A. P. L. (eds). *Mathematical Geophysics: A survey of recent developments in seismology and geodynamics*, Reidel.

Kolb, P., Collino, F., and Lailly, P., 1986, Pre-stack inversion of a 1-D medium: *Proceedings of the IEEE*, **74**, 498–508.

Lailly, P., 1983, The seismic inverse problem as a sequence of before stack migrations: In Bednar, J. B., Redner, R., Robinson, E., and Weglein, A., (eds). *Conference on Inverse Scattering: Theory and Applications*, Society of Industrial and Applied Mathematics.

Levander, A., 1988, Fourth-order finite-difference P-SV seismograms: *Geophysics*, **53**, 1425–1437. doi: 10.1190/1.1442422

Mora, P., 1987, Non-linear two-dimensional elastic inversion of multi-offset seismic data: *Geophysics*, **52**, 1211–1228. doi: 10.1190/1.1442384

Mora, P., 1988, Elastic wavefield inversion of reflection and transmission data: *Geophysics* **53**, 750–759. doi: 10.1190/1.1442510

Mora, P., 1989, Inversion = migration + tomography: *Geophysics* **54**, 1575–1586. doi: 10.1190/1.1442625

Pica, P., Diet, J. P., and Tarantola, A., 1990, Nonlinear inversion of seismic reflection data in a laterally invariant medium: *Geophysics* **55**, 284–292. doi: 10.1190/1.1442836

Sakai, A., 1998, Broad-band seismic data acquisitions for fine scale imaging and velocity determination associated with BSR: *Proceeding of the 23rd General Assembly of the European Geophysical Society*, in SE48 Gas Hydrates in Nature: Results from geophysical and geochemical studies.

Sakai, A., 1999, Velocity analysis of vertical seismic profile (VSP) survey at JAPEX/JNOC/GSC Mallik 2L–38 gas hydrate research well, and related problems for estimating gas hydrate concentration: *Geological Survey of Canada Bulletin* **544**, 323–340.

Sakai, A., 2000, Seismic studies by 2D high resolution and reconstructed quasi-3D data combined with VSPs in the eastern Nankai Trough: *Proceedings of AGU Western Pacific Geophysical Meeting*, in *EOS, AGU Transactions* **81**, 22, WP60.

Sakai, A., 2002, Velocity estimates by the nonlinear elastic wavefield inversion method: *Proceeding of the 107th SEGJ Conference*, 47–50.

Sakai, A., 2003, Frequency-cascade scheme to the elastic wavefield inversion: A strategy for low wavenumber velocity estimate and several applications: *Proceedings of the International Symposium on Recent Advances in Exploration Geophysics*, 12–21.

Sirgue, L., and Pratt, R. G., 2001, Frequency domain waveform inversion: strategy for choosing frequencies: *Proceedings of the 63rd EAGE Conference*, P014.

Tarantola, A., 1984, Inversion of seismic reflection data in the acoustic approximation: *Geophysics* **49**, 1259–1266. doi: 10.1190/1.1441754

Tarantola, A., 1986, A strategy for nonlinear elastic inversion of seismic reflection data: *Geophysics* **51**, 1893–1903. doi: 10.1190/1.1442046

Tarantola, A., 1987, *Inverse Problem Theory – Methods for data fitting and model parameter estimation*, Elsevier.

Manuscript received 1 August 2006, accepted 31 January 2007.

Appendix: Histogram class determination by Akaike's Information Criterion

In taking histograms, it is important to define classes in a statistically plausible manner. Under the assumption that the probability of the relative errors in inverted data in each class is independent, a frequency of independent data trial takes a multinomial distribution. Currently, a histogram model $M(a, r, b)$ is assumed that in the total number of classes c and frequencies n, with probability $p(i)$ and frequency $n(i)$, the number of classes at the ends are a and b and central data between the ends are classified into classes of the number of r as follows:

$$\begin{gathered} p(1) = p(2) = \cdots = p(a) = \theta(1), \\ p(a + (j-2)r + 1) = \cdots = p(a + (j-1)r + 1) = \theta(j) \\ \text{for} \quad j = 2, \ldots, (c - a - b)/r + 1 \\ p(c - b + 1) = \cdots = p(c) = \theta((c - a - b)/r + 2) \end{gathered}$$

To estimate the most probable $\theta(j)$, for $j = 1,\ldots,(c - a - b)/r + 2$, MAICE (minimum AIC) is used as the model selection criterion. AIC(a, r, b) approximates an expectation of unbiased average logarithmic likelihood and shows –2 multiplied by (maximum logarithmic likelihood of the model – the number of free parameters of the model) (Akaike, 1974).

$$\begin{aligned} \mathrm{AIC}(a, r, b) = -2 \Bigg[& \left(\sum_{i=1}^{a} n(i) \right) \log \left(\sum_{i=1}^{a} \frac{n(i)}{an} \right) \\ & + \sum_{j=2}^{(c-a-b)/r+1} \left\{ \left(\sum_{i=a+(j-2)r+1}^{a+(j-1)r} n(i) \right) \log \left(\sum_{i=a+(j-2)r+1}^{a+(j-1)r} \frac{n(i)}{rn} \right) \right\} \\ & + \left(\sum_{i=c-b+1}^{c} n(i) \right) \log \left(\sum_{i=c-b+1}^{c} \frac{n(i)}{bn} \right) \Bigg] \\ & + 2((c - a - b)/r + 1) \end{aligned} \tag{A1}$$

非線形弾性波動場インバージョンにおける最適弾性パラメタの選定についての数値解析

酒井 明男

要 旨： 非線形波動場インバージョンの有効性の検討を行う際，これまでモデルデータあるいは実データを用いて，弾性パラメタの推定が行われてきた。ただし，音響場あるいは弾性場において広帯域の弾性パラメタを推定することに困難さがあり，本手法を高周波成分に限定して用いるとする立場の研究も多い。本研究では，広帯域の弾性パラメタを推定するために，振源波形の周波数帯域を低域から広域に段階的に広げて未知の広帯域弾性パラメタを繰り返し演算の各回で同時に推定する方法を試みた（Frequency-cascade scheme with simultaneous inversion mode)。さらに未知弾性パラメタの組をいくつか取り上げ，本手法の誤差解析により，最適な組の検討を行った。それらの組は，(1) 縦波速度，横波速度および密度，(2) 縦波インピーダンス，ポアソン比および密度，ならびに(3) 縦波インピーダンス，横波インピーダンスおよび密度である。

本論文では，実坑井データ（南海トラフ）を出発モデルとした，異なる6つの1次元モデルデータならびに2次元岩石貫入モデルデータを用いて，提案の方法を非線形波動場インバージョンで実施し，以上の3つの弾性パラメタの組について誤差分布はほぼ同等で高精度であることを示した。従って，提案の方法による広帯域弾性場の非線形波動場インバージョンにより未知弾性パラメタを推定する場合，インバージョンに用いられるパラメタの組がいずれであっても，高精度の推定値が得られると結論される。すなわち，これらの数学的に等価な弾性パラメタの組は，広帯域の非線形波動場インバージョンによる未知弾性パラメタ推定においても，誤差分布の観点からはほぼ同等である。

キーワード：非線形弾性波動場インバージョン，周波数逓増技法，連立同時解法，ガスハイドレート

비선형 탄성파 파동장 역산 방법에서 탄성파 변수 세트에 관한 정보의 수치적 연구

Akio Sakai

요 약： 비선형 파동장 역산은 지하의 암석과 물성을 결정하는 물리적인 제약을 위한 탄성파 변수들을 평가하는데 강력한 방법이다. 이 논문에서는 현장자료와 2 차원 탄성파 속도 모델로부터 탄성파 속도 변화를 재구성하여 만들어낸 6 가지 탄성파 속도 모드를 제시하였다. 탄성파 반사파 자료의 정보는 종종 단파장과 장파장 성분으로 나뉘어진다. 지역검색 방법은 만약 초기모델이 실제 모델로부터 동떨어지면 장파장의 속도 변화를 측정하는데 어렵다. 그러면 송신주파수들은 낮은 대역에서 더 높은 대역들로 모델의 탄성파 변수들을 측정하기 위해 변환된다 (frequency-cascade scheme). 탄성파 변수들은 P 파와 S 파 속도가 심도에 따라 선형으로 변화는 초기 모델 가정하에 각 역산단계에서 (simultaneous mode) 계산된다. P 파와 S 파 속도 ('Vp Vs mode'), P 파 임피던스와 포와송 비 ('Ip Poisson mode'), P 파와 S 파 임피던스 ('Ip Is mode')와 같은 세가지 모드들이 탄성파 변수들의 역산을 위해 얻어진다. 각 탄성파 역산 단계에서 밀도값들은 세가지 가정하에 개선(update)된다. 탄성파 모델을 위한 각 변수 세트들에서 역산의 정확도를 평가한 결과 Vp Vs 모드와 Ip Poisson 모드 사이에 별다른 역산 차이는 없었다. Ip Is 모드들에 대해서도 같은 결론이 예상된다. 이러한 결과들은 전 파장에 걸친 탄성파 파동장 역산의 견고한 기초를 제공한다.

주요어： 비선형 탄성파 파동장 역산, 계단식 주파수 이동 방법, 동시 모드, 가스하이드레이트

石油資源開発(株)
〒140-0002 東京都品川区東品川 2-2-20

석유자원개발㈜